Poster presented at the
"Jahrestagung der Astronomischen Gesellschaft"
September 22-27, 1997, in Innsbruck

Numerical Simulations of Stellar Surface Convection along the Main-Sequence

Bernd Freytag, Matthias Steffen

Institut für Astronomie und Astrophysik der Universität Kiel,
D-24098 Kiel, F.R.G., [Freytag/Steffen@astrophysik.uni-kiel.de]

1 Abstract

We present a sequence of numerical 2D radiation hydrodynamics (RHD) models of the surface convection zones of main-sequence stars with effective temperatures between $4\,500\,\mathrm{K}$ and $9\,000\,\mathrm{K}$. From these models we

- calibrate the mixing-length parameter α, appropriate to reproduce, with mixing-length models, the adiabat of the convection zone derived from the RHD models.
- determine the variation of the typical horizontal extent of the granules with spectral type.
- measure the magnitude of the photospheric acoustic energy flux along the main-sequence.

2 Numerical simulations

Based on 2D numerical radiation hydrodynamics calculations of time-dependent compressible convection, a variety of stellar surface convection zones has been studied. The equation of state accounts for the ionization of H and He. The non-local equation of radiative energy transport is solved along a number of representative rays, assuming LTE. Grey or frequency-dependent opacities can be used (for details see Ludwig et al. 1994)

Two different lower boundary conditions are applied: For models that completely accommodate a shallow convection zone, a closed lower boundary is used (Figs. 1, 2, 3). Models with solar-like deep convection zones need a sophisticated open lower boundary condition that allows the free in- and outflow of material (Figs. 4, 5, 6). Here the inward mass flux is adjusted to keep the mass inside the model constant and the entropy of the inflowing material is regulated as to keep the long-term average of the total radiative flux at the top equal to $\sigma T_{\rm eff}^4$.

Simulations in 2D have the advantage of allowing the generation of a representative grid of models with reasonable computational effort. Nevertheless, only 3D simulations can in principle include all possibly important physical effects. **Therefore a new 3D code is currently under construction.**

3 Results

3.1 Examples: Dynamics of the convective flow

Typical examples of flow patterns are presented in Figs. 1 to 6. The velocity field is indicated by short pseudo-streamlines. Contour lines and colour indicate the temperature T, small tick marks at the top and the right show the positions of the computational grid points. Four columns at the right show some horizontally averaged quantities: the sign of the vertical entropy gradient, the sign of the vertical enthalpy flux, the natural logarithm of the mean gas pressure, and the logarithm of the optical depth. A positive entropy gradient defines a convectively stable region and a negative one an unstable zone. The origin of the height scale on the left corresponds to the layer with $\log \tau = 0$. The height z is counted upward. The lower boundary is closed (Figs. 1, 2, 3) or open (Figs. 4, 5, 6). The top is always transmitting for waves. The lateral boundary conditions are periodic. The chemical composition is solar. Grey opacities are used.

The turbulent dynamics is governed by fast, narrow, cool downflows extending from the stellar surface into great depth. They are surrounded by broad hotter regions with small upward velocities. New downdrafts are created in quiet regions by convective instability. They are advected horizontally until they merge with others, thereby producing deep reaching plumes and strong emission of sound waves.

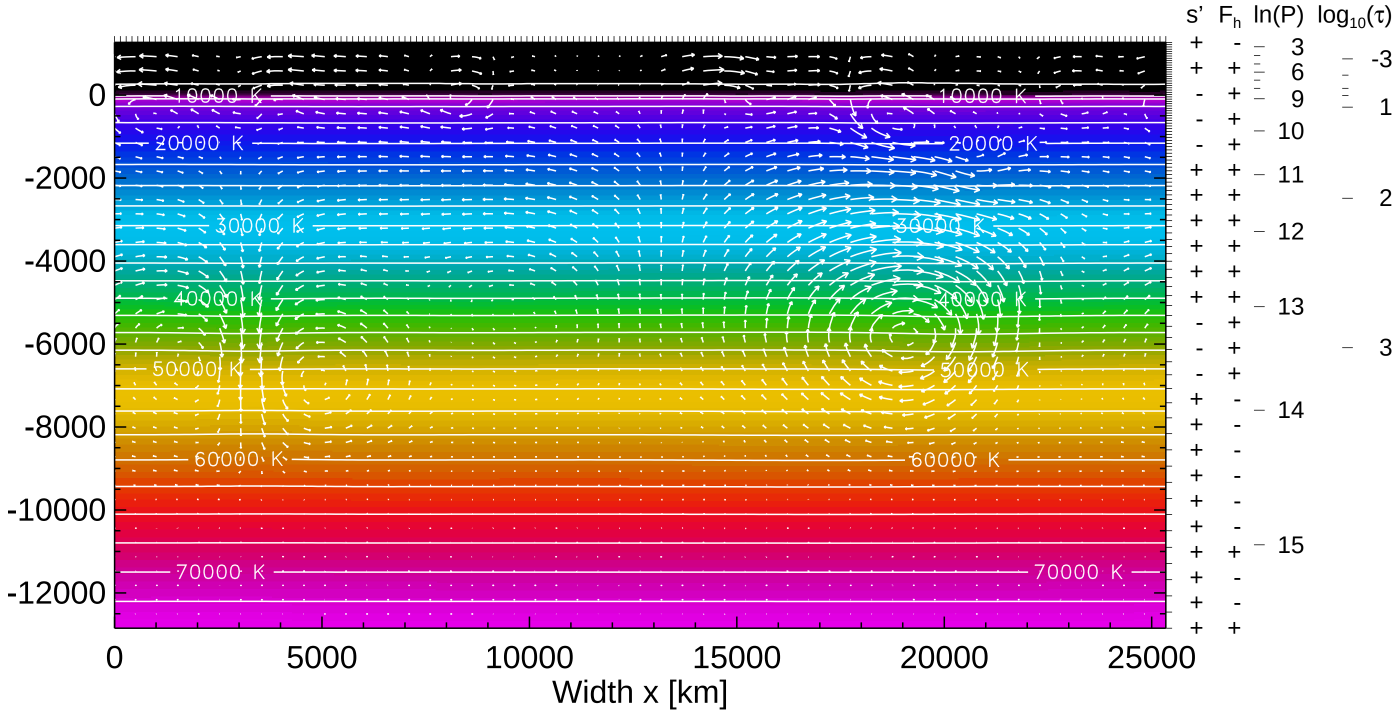

Figure 1: Snapshot of a main-sequence A star model (AT90g44N4) with $T_{\rm eff}$=9 000 K, $\log g$=4.40, 182×95 grid points, $v_{\rm max}\sim$3 km/s, $F_{h,\rm max}\sim0.001\,\sigma T_{\rm eff}^4$ (lower cz), $F_{h,\rm max}\sim0.0001\,\sigma T_{\rm eff}^4$ (upper cz). Convective energy transport and influence on the thermal structure are negligible. Radiation transport is dominating. Convective velocities are small. Nevertheless, convective mixing in both connected convection zones, including large overshoot regions, is able to counteract element separating processes e.g. due to gravitational settling.

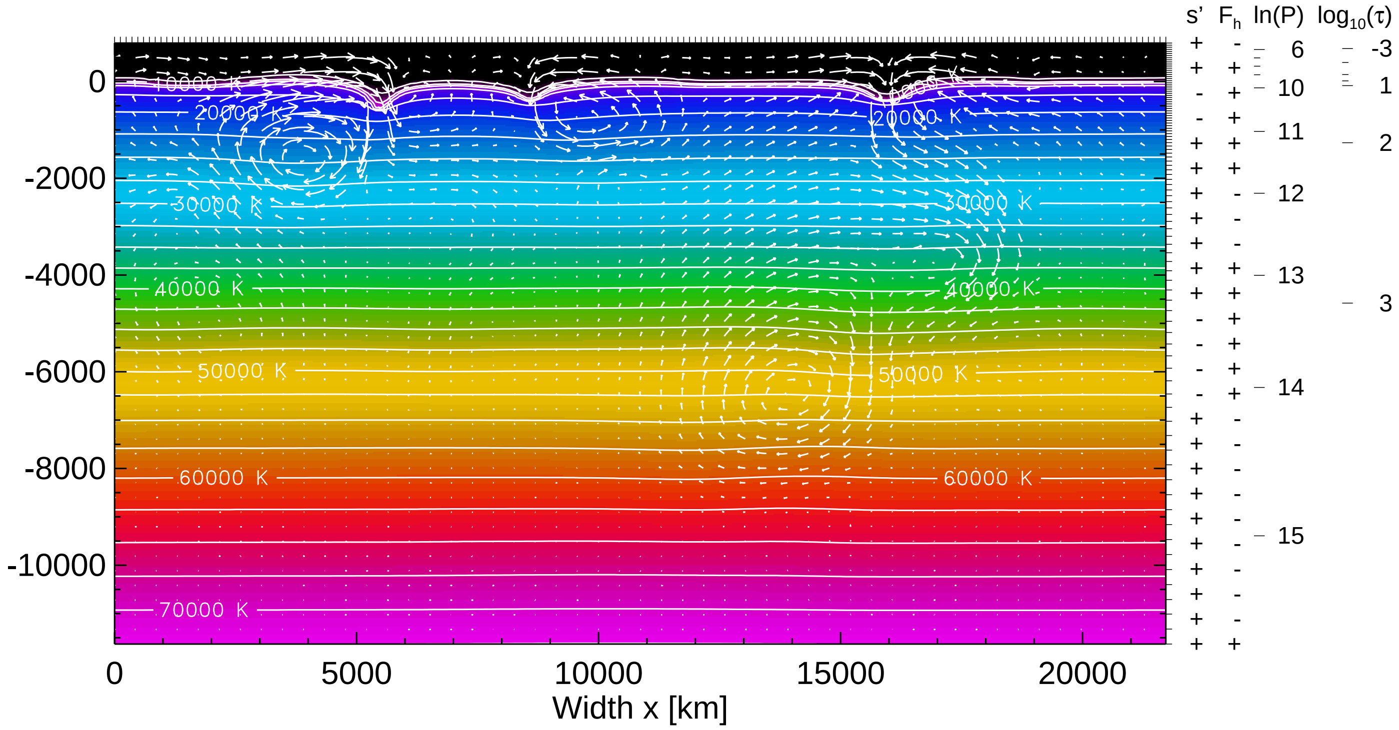

Figure 2: Snapshot of a main-sequence A star model (at80g44n7) with $T_{\rm eff}$=8 000 K, $\log g$=4.40, 182×95 grid points, $v_{\rm max}\sim$16 km/s, $F_{h,\rm max}\sim0.01\,\sigma T_{\rm eff}^4$ (lower cz), $F_{h,\rm max}\sim0.1\,\sigma T_{\rm eff}^4$ (upper cz). The convective energy flux starts to become significant. Convective velocities are considerably larger than at $T_{\rm eff}$=9 000 K.

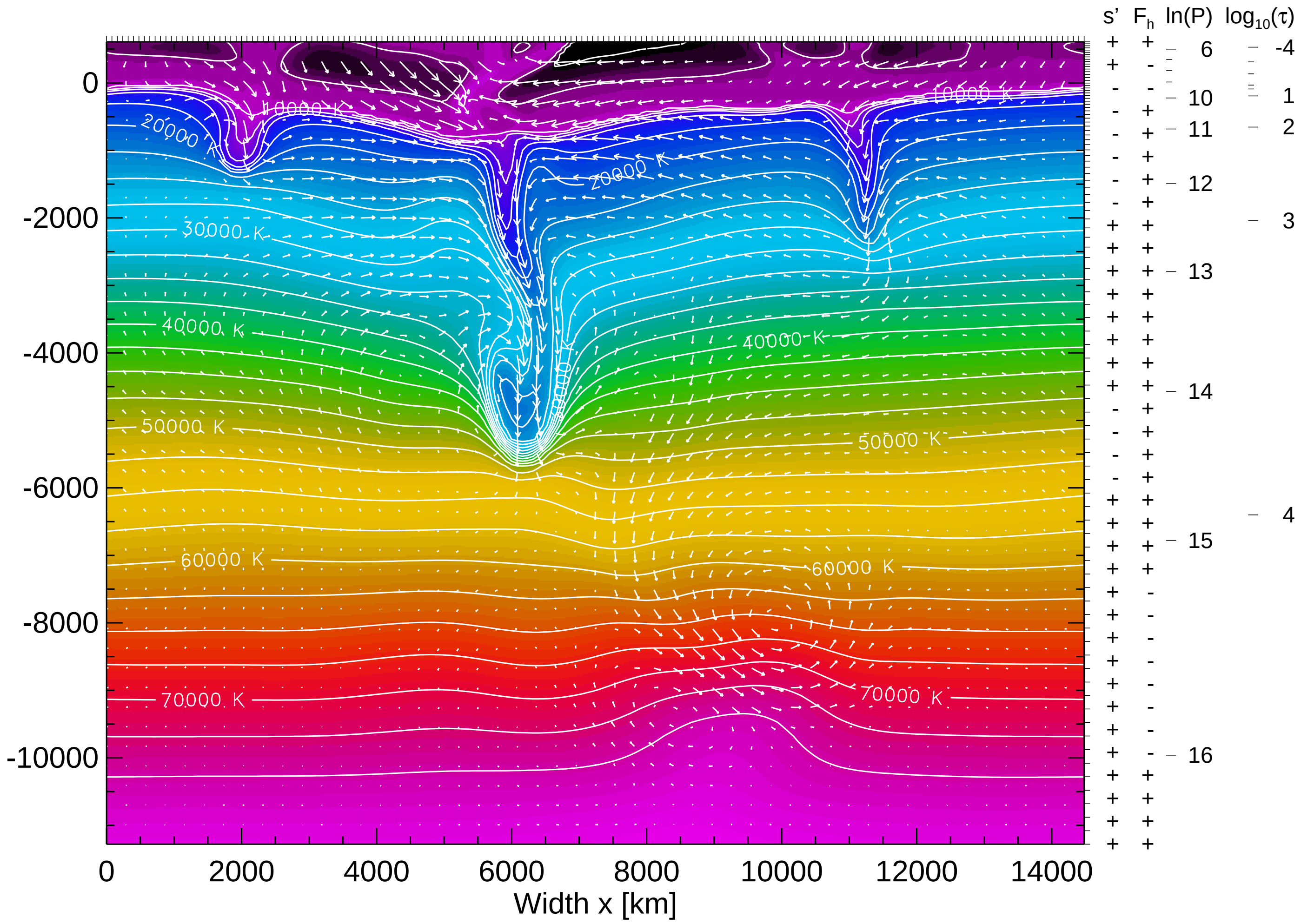

Figure 3: Snapshot of a main-sequence F star model (at70g44n2) with $T_{\rm eff}{\sim}7\,270\,\mathrm{K}$, $\log g{=}4.44$, $182{\times}95$ grid points, $v_{\rm max}{\sim}29\,\mathrm{km/s}$, $F_{h,\rm max}{\sim}1\,\sigma T_{\rm eff}^4$. Plumes, reaching from the surface into the lower instability zone, dominate the velocity field. Supersonic flows are omnipresent. Noticeable velocities and temperature fluctuations near the bottom of the model indicate that the lower boundary should preferably be located at a still larger depth.

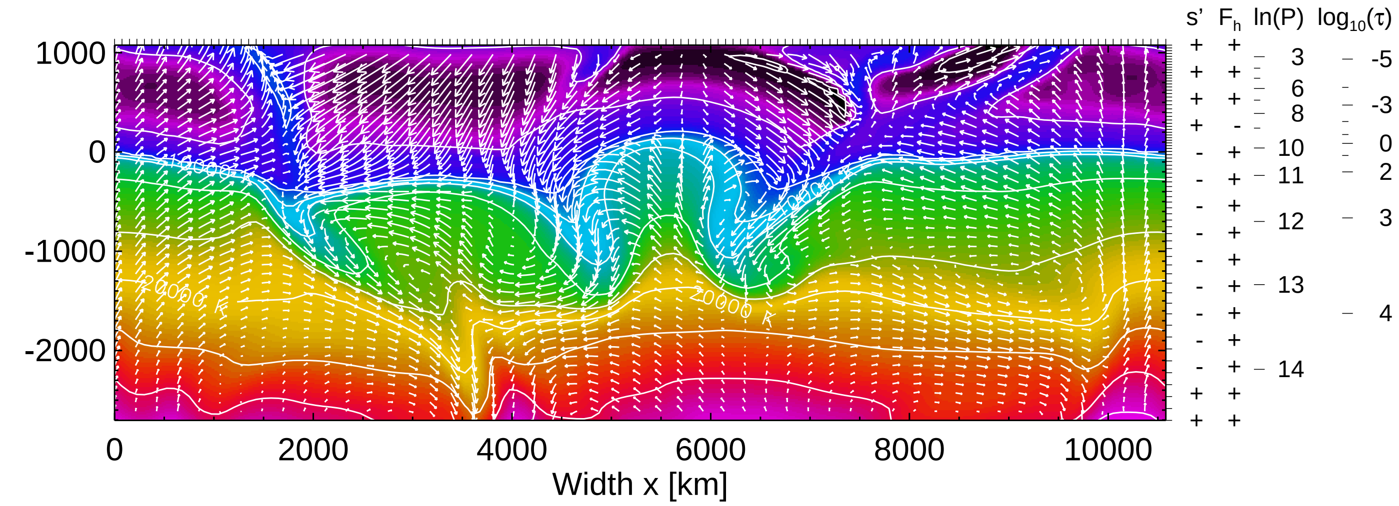

Figure 4: Snapshot of a main-sequence F star model (gt70g44n2) with $T_{\rm eff}{=}7\,000\,\mathrm{K}$, $\log g{=}4.44$, $142{\times}71$ grid points, $v_{\rm max}{\sim}25\,\mathrm{km/s}$, $F_{h,\rm max}{\sim}1\,\sigma T_{\rm eff}^4$. Only the upper part of the convection zone is contained in the computational volume. In the subphotospheric layers radiation becomes unimportant while the flow becomes more and more turbulent.

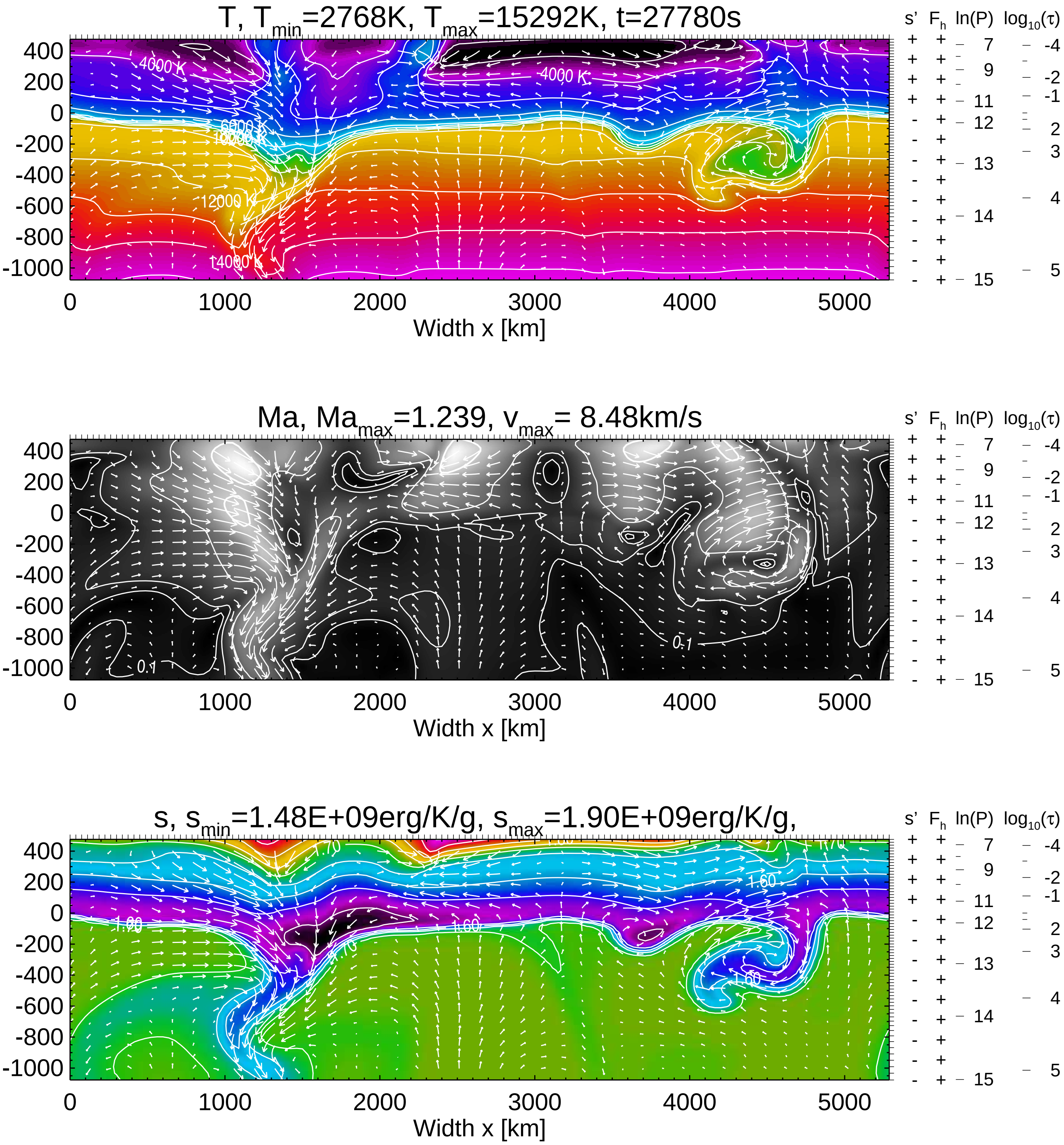

Figure 5: Snapshot of a G star model (GT57g44N1) with $T_{\rm eff}$=5 770 K, log g=4.44 (Sun), 142×71 grid points. Contour lines and colour indicate the temperature T (upper panel), the Mach number Ma (center), and the specific entropy s (lower panel).

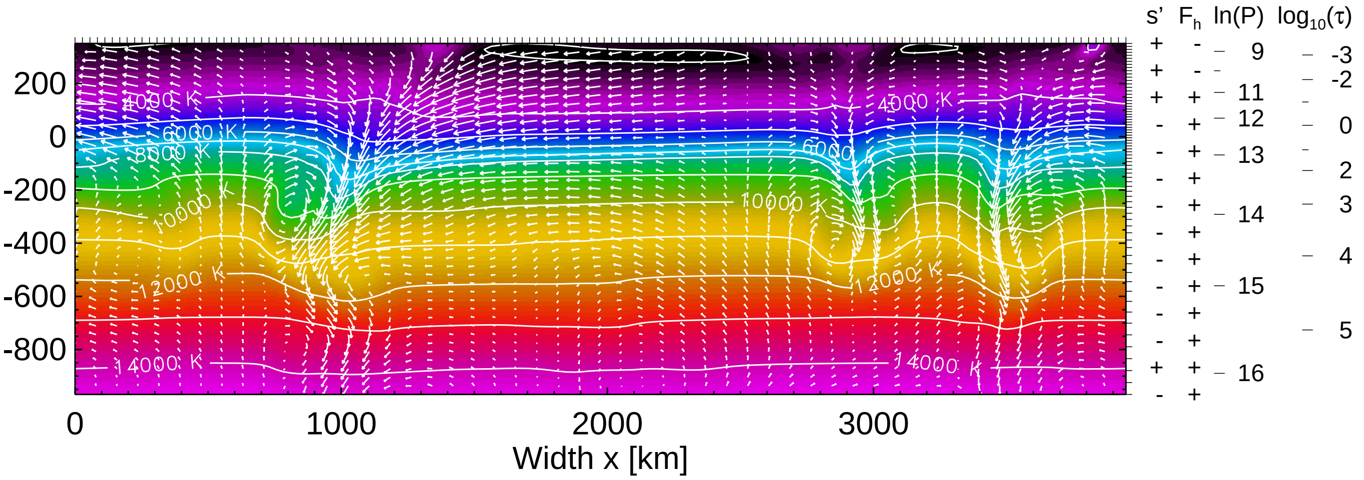

Figure 6: Snapshot of a main-sequence K star model (gt45g44n7) with $T_{\rm eff}$=4 500 K, $\log g$=4.44, 142×71 grid points, $v_{\rm max}$∼7 km/s, $F_{h,\rm max}$∼1 $\sigma T_{\rm eff}^4$. The velocities are smaller and the temperature field is smoother than in the hotter models. Nevertheless, in the subphotospheric layers convection is extremely efficient.

3.2 Typical size of the granulation

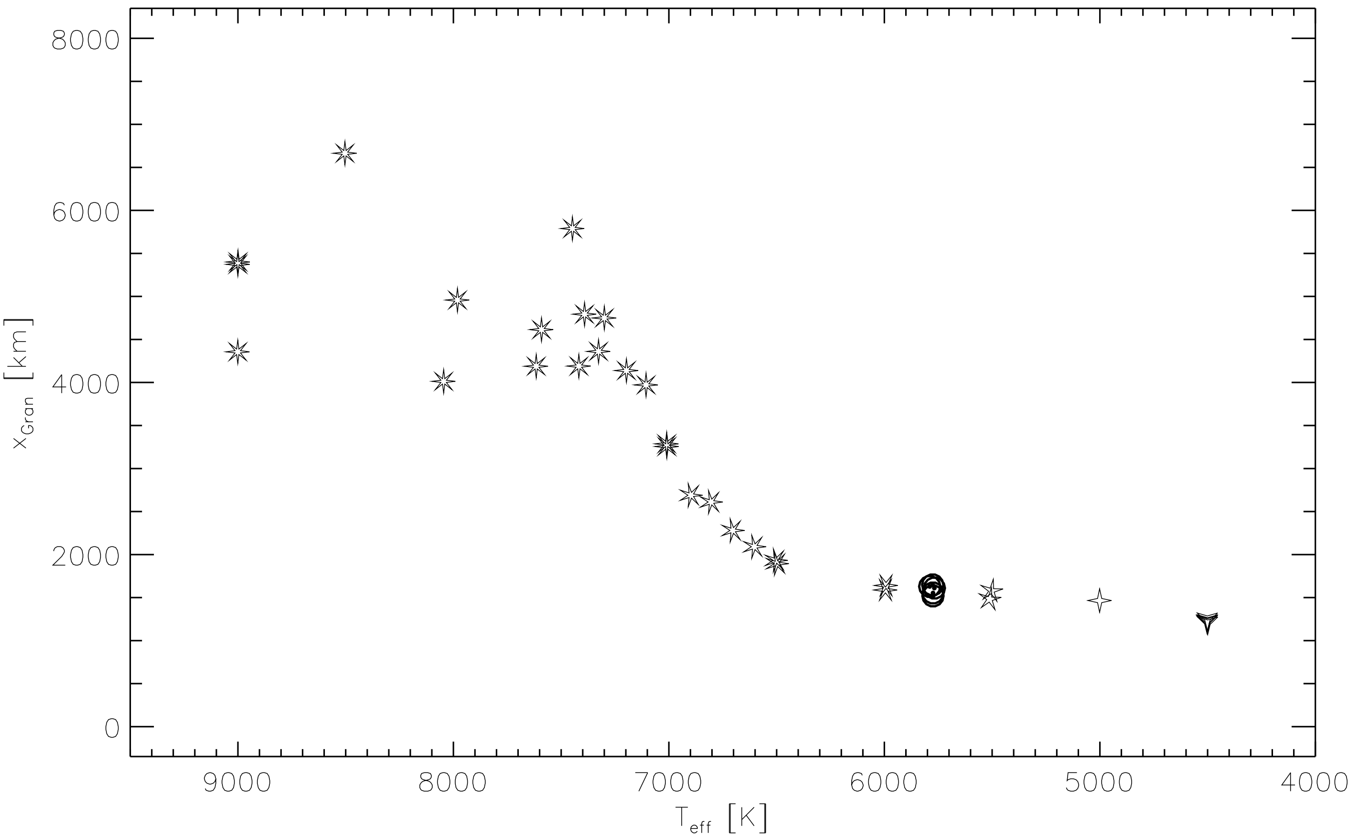

Figure 7: Typical horizontal extent x_{Gran} of a granule as function of the effective temperature T_{eff}. Gravity $\log g$=4.40-4.44. Each symbol indicates one RHD model. The Sun is marked by the $\odot$ symbols.

The typical size of a granule is defined as the mean horizontal distance between two neighbouring downdrafts stronger than a certain limit. In this way the influence of eddies and waves and – unfortunately – the contribution of small granules is suppressed.

Below 6 500 K the size variation is completely explained by the variation of the characteristic pressure scale height due to the change in effective temperature ($x_{\text{Gran}} \sim H_p$).

From 6 500 K towards higher effective temperature radiative energy exchange becomes more and more important by smoothing out small structures, thus favouring larger cells.

3.3 Effects of surface convection on the stellar interior

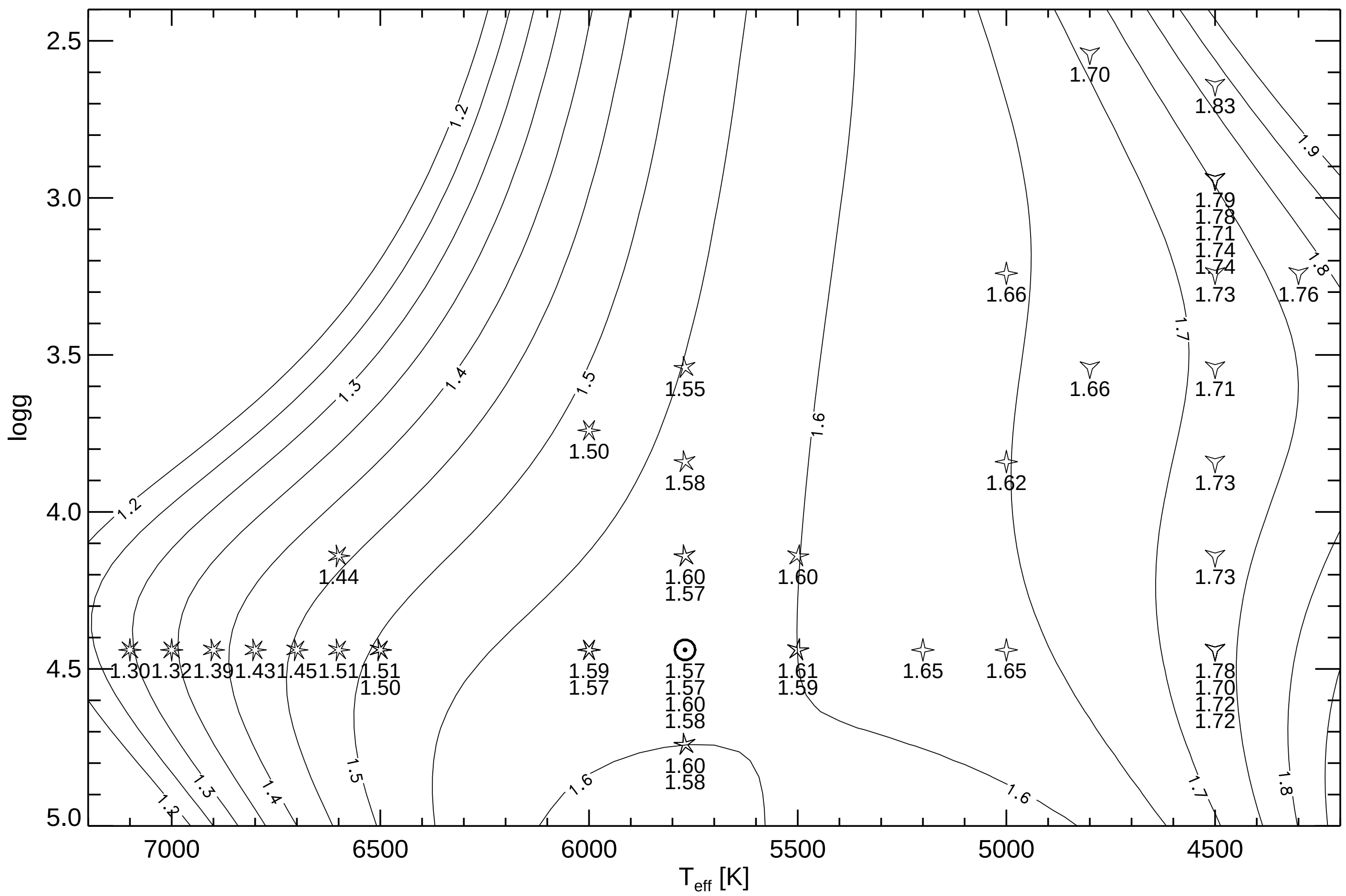

Figure 8: Calibrated mixing-length parameter α for solar composition as function of the effective temperature T_{eff} and gravity $\log g$. Each symbol indicates one RHD model. The Sun is marked by the $\odot$ symbol.

Assuming that the value of the entropy plateau can be directly identified with the entropy of the deep, adiabatic convective layers, it is possible to calculate MLT models with a corresponding entropy of the deep adiabat and to derive in this way an effective mixing-length parameter α (Steffen 1993). In the main-sequence phase the effective α for the Sun is a constant close to 1.60. But it increases slightly during the evolution towards the red giant branch (upper right).

Currently, our model grid is extended towards lower metallicities. For lower metallicities the mixing-length parameter depends in a more complex way on effective temperature and gravity than for the solar metallicity case shown in Fig 8. The final goal of the α-calibration is to derive the function $\alpha(T_{\mathrm{eff}}, \log g, Z)$ which can be used in stellar evolution calculations. This allows the investigation of the influence of such an α-variation on the age determination of globular clusters.

3.4 Effects of surface convection on the outer atmosphere

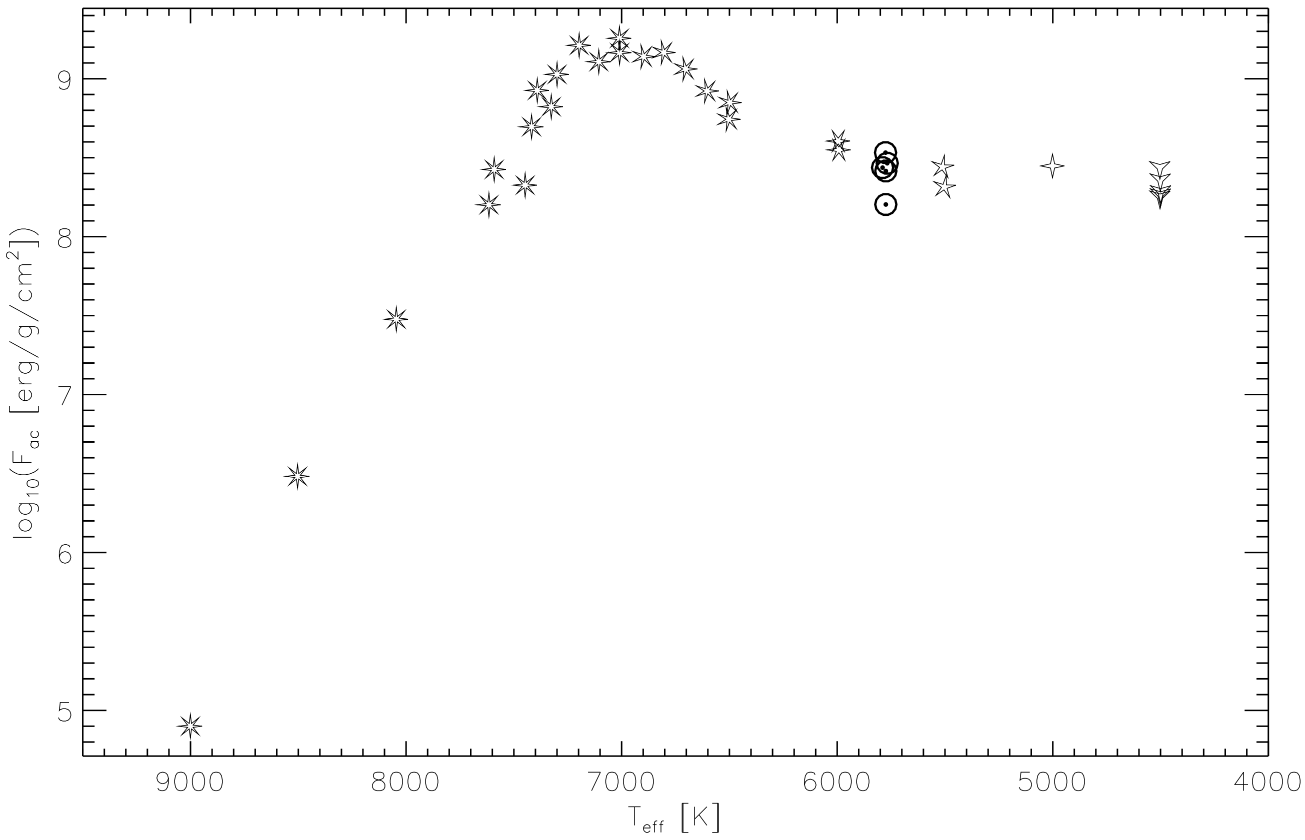

Figure 9: Acoustic flux F_{ac} at the optical depth $\log\tau$=-2 as function of the effective temperature T_{eff}. Gravity $\log g$=4.40-4.44. Each symbol indicates one RHD model. The Sun is marked by the $\odot$ symbols.

The acoustic flux can be computed directly from the numerical models (Steffen 1994). Unfortunately, we do not find a constant acoustic energy flux flowing from the convectively unstable regions through the photosphere and the top of the model. Instead, the acoustic flux decreases exponentially with height, making it difficult to decide from our photospheric models alone, which part might be able to reach the chromosphere contributing to its heating.

By selecting arbitrarily the point $\log\tau$=-2 in the photosphere the acoustic flux shows a dependence on effective temperature as shown in Fig. 9. Solar-type stars all show a similar acoustic energy production rate. Thus there is so far no indication that a drastic change in the convective sound production might be responsible (in some way) for the disappearance of coronae at low effective temperatures (Haisch et al. 1991).

References

Haisch B., Schmitt J.H.M.M., Rosso C., 1991, ApJL 383, 15-18

Ludwig H.-G., Jordan S., Steffen M., 1994, A&A 284, 105

Steffen M., 1993, in "Inside the stars", IAU Colloquium 137, eds. W. Weiss, A. Baglin, Astron. Soc. Pacif. Coonf. Series Vol. 40, p. 300

Steffen M., 1994, in "Solar Magnetic Fields", eds. M. Schüssler, W. Schmidt, Cambridge University Press, p. 294-297